Quantum Dot−Block Copolymer Hybrids for Low Scattering Luminescent Solar Concentrators

Kayla C. Koch, Daniel Korus, Justin Doyle, Megan Plummer, Meredith Boxx, Hla Win-Piazza, Stephen McDowall, David L. Patrick, and David A. Rider*

Cite This: *ACS Appl. Polym. Mater.* 2022, 4, 3283−3293
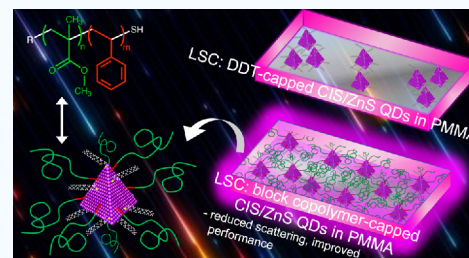
Read Online

ACCESS | Metrics & More | Article Recommendations | SI Supporting Information

ABSTRACT: Luminescent solar concentrators (LSCs) use down-converting phosphors embedded in a transparent waveguide to absorb sunlight, trap luminescent photons by total internal reflection, and deliver high irradiance, narrowband output light for driving photovoltaic, photochemical, and other solar energy converters. Quantum-dot-based (QD) LSCs are typically affected by several optical loss mechanisms including the loss of a fraction of guided light during transport to the concentrator edges through scattering from QD aggregates. Although the recent introduction of large effective Stokes shift QD luminophores for LSC applications has helped address several shortcomings associated with previous generations of organic and inorganic dyes, including improved solar

spectrum matching, photostability, and photoluminescence quantum yield, achieving low light scattering at technologically relevant QD loadings in commercially deployed polymers such as poly(methyl methacrylate) (PMMA) remains challenging. Herein, we study the concept of applying QDs bearing polymer ligands matching the composition of the LSC matrix to reduce aggregation and the resulting parasitic waveguide losses caused by scattering. We report the synthesis and characterization of a thiol-terminated PMMA-based ligand and its successful ligand exchange reaction with copper indium disulfide/zinc sulfide (CIS/ZnS) QDs. QDs bearing PMMA ligands are then applied as down-converting phosphors embedded in a PMMA waveguide. The resulting QD-based LSCs were found to have lower optical scattering with higher loading as a result of reduced aggregation in the devices.

KEYWORDS: luminescent solar concentrator, quantum dot, nanocrystal, ligands, block copolymer, polymer composites, solar concentration

INTRODUCTION

Polymer−semiconductor nanocrystal (NC) composites are employed as optically active elements in a wide range of applications, such as downshifting layers for lighting and displays,[1−3] scintillation detectors,[4] fiber lasers,[5] amplified spontaneous emission sources,[6,7] hybrid organic/inorganic light-emitting diodes,[8−10] and luminescent solar concentrators (LSCs).[11−13] The latter have emerged as one of the most promising approaches for practical building-integrated solar energy harvesting because LSCs concentrate diffuse as well as direct sunlight, are tolerant to partial shading, are semi-transparent, and can be architecturally integrated into building facades or windows.[14,15] LSCs theoretically enable conversion efficiencies superior to other concentrator designs,[16−19] but achieving high optical gain requires a thin (∼1 mm), large area (∼1 m²) form factor resulting in long optical path lengths, making minimization of optical losses critical. All LSCs are affected by four principal optical loss mechanisms:[19−22] (1) only a fraction of incident sunlight is absorbed, determined by the luminophore absorption spectrum; (2) only a fraction of absorbed sunlight is re-emitted, depending on luminophore photoluminescent quantum yield (PLQY, Φ); (3) only a fraction of this emitted light is captured in guided modes (e.g., ∼75% in a planar waveguide with refractive index $n \sim 1.5$),
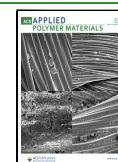
with the remainder lost to escape cones defined by Snell's law; and (4) a fraction of guided light is lost during transport to the concentrator edges by propagation losses. Losses (2) and (3) are compounded by luminophore self-absorption resulting from overlap of absorption and emission bands.

LSCs require luminophores with a broad absorption profile, a high PLQY, and a large Stokes shift.[21] Over the past 40 years a wide variety of candidate materials have been investigated, including small molecule and polymer fluorophores,[23−26] lanthanide-doped glasses,[27−31] and various types of semi-conductor nanocrystals (types I and II,[32−38] "giant shell",[39−41] and "dot-in-rod"[42] and doped compositions such as Mn^{2+}:ZnSe, Mn^{2+}:$Cd_xZn_{1−x}$Se, CuInSe, and Cu^+:CdSe).[43−48] Among these phosphors, $CuInS_2$/ZnS (CIS/ZnS) QDs and related compositions are perhaps the most promising identified so far for LSC applications. They combine high PLQY and broadband absorption well matched to the solar spectrum with

an extremely large effective Stokes shift (≥400 meV, Figure 2), resulting in small Förster radii and minimal self-absorption. Consequently, elastic light-scattering losses, as opposed to the loss-compounding effects of self-absorption, are expected to be most prominent in composite waveguides incorporating high QD loading. Recent work suggests significant improvements in optical gain should be possible in large LSCs if these light-scattering losses can be reduced.[49]

Previous work has shown that utilizing a polymer brush layer on nanoparticles is particularly effective in the management of aggregation because of the tailored compatibility of the QD with the polymer matrix and the tuning of the interparticle interaction potential.[50] Herein, we design and synthesize a thiol-terminated poly(methyl methacrylate) ligand appropriate for a ligand exchange reaction with native ligand dodecanethiol-rich CIS/ZnS QDs and integrate them into poly-(methyl methacrylate) (PMMA)-based LSCs. Finally, we test these LSCs and compare their relative efficiencies to LSCs fabricated without polymer functionalized QDs and also to other LSC architectures published in the literature.

■ EXPERIMENTAL SECTION

Materials. Methyl methacrylate, n-propylamine, styrene, and sodium bisulfite were all used as purchased from Acros Organics. Cumyl dithiobenzoate was used as purchased from Ark Pharm. Hexanes, 2,2′-azobis(2-methylpropionitrile) (AIBN), indium acetate, 1-octadecene, 1-dodecanethiol, trioctylphosphine, sulfur powder, zinc stearate, copper iodide, 3-(trimethoxysilyl)propyl methacrylate, photoinitiator 2,2-dimethoxy-2-phenylacetophenone (Irgacure 651), and benzene were all used as purchased from Sigma-Aldrich. PMMA beads (MW = 25000 Da) were used as purchased from Polysciences. Reagent grade ethanol (EtOH), isopropyl alcohol (IPA), and tetrahydrofuran (THF) were purchased from Fisher Chemical. Reagent grade toluene was used as received from Macron Inc. B270 glass was purchased from SI Howard Glass and used for LSC fabrication.

Methods. A Bruker AVANCE-III HD 500 MHz NMR spectrometer was used to collect all ^{1}H NMR spectra. Specifications for standard 2D NMR NOESY and DOSY programs are included in the Supporting Information (Table S1). A Malvern GPCMax instrument operated with a refractive index (RI) detector and THF eluent flowing at a rate of 1 mL/min was used for gel permeation chromatography (GPC). A Jasco V-670 UV/vis was used for optical spectroscopy. A Horiba Fluorolog model FL3-21 connected via liquid light guide to an integrating sphere was used to collect LSC and QD fluorescence. TEM images were taken with a Phillips CM100 outfitted with an Olympus Morada. XRD diffractograms were acquired by using a Rigaku MiniFlex 6G.

Thermal Analysis. All weight changes and char yield studies were conducted with a TA Instruments Q500 thermogravimetric analyzer. The samples were held at an isotherm for 15 min at 100 °C and then ramped from 100 to 700 °C at 10 °C/min under a nitrogen atmosphere. A TA Instruments Q100 differential scanning calorimeter (DSC) was used for all glass transition studies. All samples were scanned at a rate of 5 °C/min with an amplitude of ±0.531 °C in a heat−cool−heat run from 30 to 260 °C and back to 30 °C. When possible, the inflection point in the DSC curve was used to calculate the glass transitions for certain samples.

Preparation of Copper Indium Disulfide/ZnS Core/Shell QDs [CIS/ZnS QDs]. CIS QD cores were synthesized following a procedure adapted from Li et al.[51] A 50 mL three-necked flask containing copper(I) iodide (0.320 g, 1.68 mmol), indium(III) acetate (0.584 g, 2.00 mmol), and 1-dodecanethiol (10.0 mL, 42.7 mmol) was stirred and degassed three times at room temperature followed by heating to 100 °C under nitrogen until all solid precursors were dissolved. Raising the temperature to 230 °C initiated core growth, which was allowed to proceed for 10 min following the onset

of visible color change. Core growth was arrested by a thermal quench using a room temperature water bath.

A ZnS shell overgrowth solution was prepared by sonicating zinc stearate (2.530 g, 4.001 mmol) and 1-octadecene (ODE) (40.0 mL, 125 mmol) for several hours. Crushed sulfur (S_8) powder (0.128 g, 0.5 mmol) was separately dispersed in trioctylphosphine (TOP) (10.0 mL, 22.4 mmol) via sonication under nitrogen. The zinc stearate−ODE solution was then degassed and purged three times with nitrogen at room temperature and mixed with the sulfur−TOP solution. The above CIS core solution was diluted with ODE (40.0 mL, 125 mmol), transferred to a 250 mL round-bottom flask, and degassed three times, purging with nitrogen while stirring. The shelling solution was added dropwise at a rate of 15 mL/h at 210 °C, and the mixture allowed to cool to room temperature.

The resulting core/shell CIS/ZnS QDs were purified via repeated precipitation resuspension with EtOH and IPA, followed by redispersion in hexanes. This was followed by loading a toluene solution of the CIS/ZnS nanocrystals (∼100 mg/mL) into a size exclusion column (19 mm ID, 10 cm long) packed with BioRad biobead X1 resin with toluene as the eluent.

Synthesis of α-Phenyl-ω-dithiobenzoate-PMMA. The synthesis of α-phenyl-ω-dithiobenzoate-PMMA was adapted from Xu et al.[52] A two-neck 100 mL round-bottom flask was fitted with a condenser and a septum followed by dissolving 5.12220 g (0.0188 mol) of cumyl dithiobenzoate (CDB) and 1.23012 g (0.00749 mol) of 2,2′-azobis(2-methylpropionitrile) (AIBN) in 9.3 mL of benzene. The atmosphere was purged with nitrogen for 30 min while stirring with a stir bar. After degassing, 15.80 mL (0.1483 mol) of distilled methyl methacrylate (MMA) was added to the flask via syringe and submerged in an oil bath at 60 °C while stirring for 24 h. The flask was then removed from the oil bath and quenched in liquid nitrogen to arrest polymerization. The resulting product was a dark purple viscous liquid. Tetrahydrofuran (THF) was added in small amounts to reduce viscosity and the resultant liquid was precipitated into 10-fold hexanes three times. Excess hexanes were decanted, and the product was dried under vacuum overnight. After two additional precipitation steps and vacuum drying overnight, 14.6380 g of α-phenyl-ω-dithiobenzoate-PMMA was recovered for 87.28% yield.

Synthesis α-Phenyl-ω-dithiobenzoate-PMMA-b-PS Block Copolymer (BCP). A 100 mL two-neck round-bottom flask was fitted with a condenser and a septum; 13.70995 g of the previously synthesized and purified α-phenyl-ω-dithiobenzoate-PMMA and 0.42042 g (2.5603 mmol) of AIBN were dissolved in 40 mL of benzene. The atmosphere was purged with nitrogen for 30 min while stirring. Distilled styrene (4.10 mL, 0.0358 mol) was added via syringe, and the reaction flask was submerged in an oil bath at 60 °C for 24 h while maintaining stirring. The flask was removed, and the reaction was quenched in liquid nitrogen to arrest polymerization. The resulting product was a vibrant pink liquid. The product was precipitated into 10-fold hexanes to THF once. Excess hexanes were decanted, and the product was left to dry under vacuum overnight, yielding 14.93231 g of α-phenyl-ω-dithiobenzoate-PMMA-b-PS (86.09% yield).

Synthesis of α-Phenyl-ω-thio-PMMA-b-PS BCP Ligand. Thiol-terminated PMMA-b-PS BCP was synthesized in a similar manner as Xu et al.[52] In a 500 mL round-bottom flask fitted with a septum, 13.85247 g of α-phenyl-ω-dithiobenzoate-PMMA-b-PS and 5 drops of aqueous sodium bisulfite were dissolved in 100 mL of THF. The atmosphere was purged with nitrogen and degassed for 30 min while stirring with a stir bar. Using a syringe, we added 36.4 mL (0.443 mol) of n-propylamine to the flask. The color of the solution slowly changed from a bright pink to a pale yellow over 3 min. This solution was left stirring for 6 h at room temperature. To purify, the product was filtered through glass wool and precipitated into cold hexanes (∼10-fold hexane to THF by volume). Excess hexanes were decanted, and the product was dried under vacuum overnight. The dried product was dissolved in THF and precipitated into cold hexanes three more times in the same 10-fold hexanes to the THF ratio. Again, excess hexanes were decanted, and the remaining product

was left to dry under vacuum overnight. The final α-phenyl-ω-thio-PMMA-b-PS BCP was recovered with 80.68% overall yield.

Ligand Exchange with α-Phenyl-ω-thio-PMMA-b-PS BCP Ligand and CIS/ZnS QDs. We followed a ligand exchange procedure adapted from Draaisma et al.[53] In a typical exchange reaction 0.175 g of DDT-capped QDs and 1.745 g of α-phenyl-ω-thio-PMMA-b-PS BCP were thoroughly mixed by codissolving in ~5 mL of THF. The solution was fully concentrated by rotary evaporation of the solvent, and the resulting QD/BCP mixture was heated under nitrogen at 140 °C for 5 h. Afterward, the melt mixture was dissolved in toluene and purified by size exclusion chromatography as described above, yielding 0.327 g of α-phenyl-ω-thio-PMMA-b-PS BCP-capped QDs.

LSC Fabrication. LSCs were fabricated from two pieces of 75 × 75 × 1 mm³ B270 glass formed into a hollow shell by using a 2 mm wide ×1 mm thick transparent adhesive acrylic gasket around the perimeter, yielding LSCs having a geometric gain $G = 6.25$, where G is the ratio of facial to edge area. The inner glass surfaces were first brush-coated with a 0.0042 M solution of 3-(trimethoxysilyl)propyl methacrylate to promote adhesion. The empty LSC shell was purged with N_2 and filled by using a syringe through a 0.45 μm PTFE filter with a mixture of QDs dispersed in methyl methacrylate (MMA), PMMA, and Irgacure 651 photoinitiator. This solution was prepared in three steps: first, 2.726 g of PMMA beads (25000 Da, PolySciences) was dissolved in 4 mL of MMA by stirring overnight. Next a solution containing varying amounts of QDs in 3.74 mL of MMA was prepared by sonication until homogeneous, typically requiring about 20 min. Finally, the latter was passed through a 0.45 μm PTFE filter and combined with the former, along with 0.0146 g of photoinitiator, and the solution was vigorously stirred for 5 min and degassed before being immediately introduced into the hollow LSC glass shell. After filling, LSCs were cured under UV light for a total of 40 min, flipping every 5−10 min to achieve uniform exposure. Afterward, the edges of the LSC were sealed with Norland 63 optical adhesive, which was also cured under UV exposure.
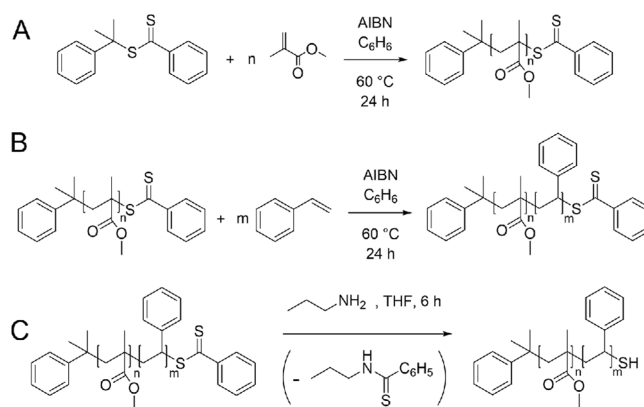
Characterization of Attenuation in Prototype LSCs. Using the method described in ref 49, we estimated the attenuation coefficients for the LSCs (with dimensions defined above) fabricated with BCP-capped QDs, which can then be compared to attenuation coefficients estimated by using the same protocol for devices incorporating DDT-capped CIS/ZnS QDs, which have been presented earlier (see ref 49). Briefly, the edge of the device was placed against the opening of an integrating sphere while the LSC was illuminated with monochromatic light at a small spot located a variable distance $d = 10−50$ mm away from the collection aperture. In the transverse direction, this illumination spot is central to the LSC, well away from the other edges. The remainder of the LSC perimeter was blackened with tape, and the LSC was suspended 10 cm above a matte black surface inside a blackened enclosure to suppress stray light and reflection from entering the integrating sphere from outside the LSC (the measurement practices employed are in agreement with those espoused in ref 54 which pertain to LSC characterization). Excitation was performed at a fixed wavelength $\lambda_{ex} = 650$ nm with the source intensity calibrated by a Si photodiode. Edge-emitted light collected by the integrating sphere was passed through a double monochromator and detected by a photomultiplier tube, producing a series of edge-emission spectra corresponding to increasing excitation distances. These data were then analyzed by using the model described below to compute an attenuation coefficient α (cm^{-1}) for guided light traveling within the LSC.

RESULTS AND DISCUSSION

Preparation and Characterization of α-Phenyl-ω-thio-PMMA-b-PS BCP Ligand. The reversible addition−fragmentation chain transfer (RAFT) polymerization of vinylic monomers followed by aminolysis of the resulting polymer is a widely used strategy for accessing thiol-terminated macromolecules.[55] The RAFT polymerization of methyl methacrylate (MMA) proceeds in a living manner and affords

monodisperse polymers with tunable molecular weights.[56] However, the thiol generated by aminolysis of dithioester-terminated PMMA can undergo a cyclization reaction with the penultimate MMA unit of the polymer, producing an undesired thiolactone terminus.[52] The PMMA-based thiol-terminated ligand employed in this work therefore includes a short segment of polystyrene (PS) to prevent the cyclization reaction. The synthetic steps used to produce the PMMA-based thiol-terminated ligand for L-type ligand exchange with the CIS/ZnS QDs are shown in Scheme 1. Cumyl

Scheme 1. (A) Polymerization of MMA with CDB to Yield PMMA; (B) Polymerization of Styrene into PMMA to Create a PMMA-b-PS BCP; and (C) Aminolysis of the PMMA-b-PS BCP with n-Propylamine to Yield Unimeric α-Phenyl-ω-thio PMMA-b-PS BCP

dithiobenzoate (CDB) was selected as the RAFT reagent since it is an established transfer agent for quasi-living polymerization of MMA, and it affords α-phenyl-ω-dithiobenzoyl-PMMA, where the phenyl unit can be used for molecular weight determination and quantification of concentration by ^{1}H NMR end-group analysis.[57] Gel permeation chromatography (GPC) was used to estimate the molecular weight and polydispersity indices (PDI) for the precursors to the thiol-terminated PMMA-based ligands. For the α-phenyl-ω-dithiobenzoyl-PMMA homopolymer, the integral ratio of the *para*-proton of the α-phenyl terminus ($\delta = 7.14$ ppm) to the protons of the methoxy side chains ($\delta = 3.57$ ppm) in the ^{1}H NMR spectra (Figure 1) was used to calculate the degree of polymerization, n, and therefore a molecular weight estimate of 2535 Da. This value agrees with the molecular weight estimate determined by conventional GPC ($M_n = 2358$ Da, PDI = 1.156). Upon RAFT polymerization of styrene using the aforementioned α-phenyl-ω-dithiobenzoyl-PMMA as a macro-RAFT reagent, the penultimate BCP was isolated. Based on the ratio of the intensity of the *para*-proton peak to the methoxy side chains as previously described, the resulting α-phenyl-ω-dithiobenzoyl-PMMA-b-PS yielded a molecular weight of 2860 g/mol, which was also in agreement with a conventional GPC estimate ($M_n = 2638$, PDI = 1.199). The degree of polymerization of styrene, m, was determined by ^{1}H NMR by comparing the integral values for the PS signal ($\delta = 6.66−7.37$) to that of the ultimate MMA repeat unit ($\delta = 3.41$ ppm). A typical m value of styrene for the resulting BCP was ~3.

After aminolysis, the ^{1}H NMR spectrum of the resulting BCP (see Figure 1) no longer exhibits the thiobenzoyl end-group signals ($\delta = 7.87, 7.54,$ and 7.38 ppm) or the thiolactone
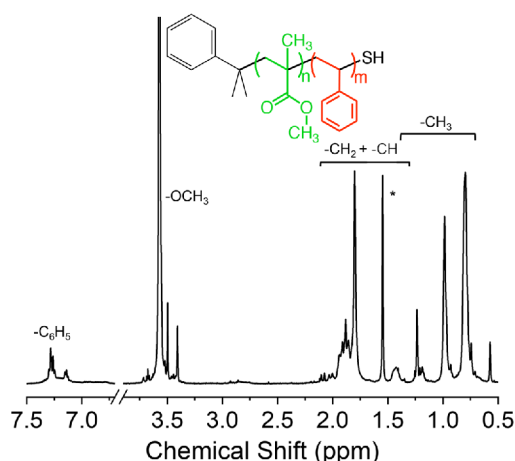
Figure 1. ^{1}H NMR of α-phenyl-ω-thio-PMMA-b-PS.

Figure 3. X-ray diffractogram of CuInS$_2$ QDs shelled with ZnS with comparison to a chalcopyrite CuInS$_2$ reference pattern (shown in red).[58]

methylene signals (δ = 2.70−2.95 ppm; see Figure S1). The resulting ^{1}H NMR spectra confirm quantitative cleavage of the RAFT-initiator end-group and the suppression of the cyclization reaction on a penultimate PMMA repeat unit.[52] The free thiols present in solution afforded some disulfide-bridged dimers of the BCPs as shown by bimodal peaks in the GPC chromatogram, each with a shoulder at an elution volume expected for dimerized BCP (see Figure S2). The M_n value of the α-phenyl-ω-thio PMMA-b-PS BCP ligand, based on the GPC elution value of the peak associated with the unimeric polymer, was found to be 2524 g/mol.

Characterization of CIS/ZnS QDs. Representative absorbance and PL spectra for α-phenyl-ω-thio-PMMA-b-PS BCP ligand-exchanged QDs are presented in Figure 2A. The spectra show an excitonic shoulder in the absorption spectrum at 515 nm and an emission peak centered at 710 nm, giving an effective Stokes shift of 420 meV. QD PLQY measured in toluene increased from ∼10% prior to shelling to 40−75% after growth of the ZnS shell. Absorbance and emission profiles were largely unaffected by ligand exchange, but PLQY typically decreased by 10−15%. The ZnS-shelled CIS QDs possess a tetrahedral shape with an average edge length of 4.1 nm measured by TEM (Figure 2B and Figure S3).[51] X-ray diffraction (XRD) analysis of CIS cores shows reflections from (112), (220), and (312) planes consistent with a hexagonal (wurtzite) crystal structure.[58] Upon shelling, these reflections undergo a subtle shift consistent with lattice strain introduced by ZnS shell overgrowth (Figure 3).[59]
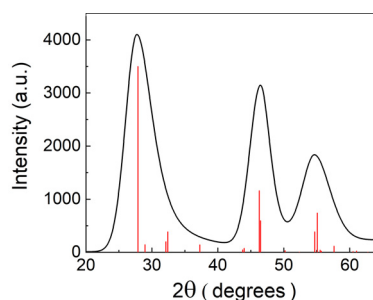
1D and 2D ^{1}H NMR Characterization of DDT-Capped and α-Phenyl-ω-thio-PMMA-b-PS BCP-Capped CIS/ZnS QDs. The synthesis of the CIS/ZnS core/shell QDs includes stearic acid, trioctylphosphine, octadecene, and 1-dodecanethiol (DDT) as ligands and purification was accomplished by precipitation resuspension followed by size exclusion chromatography before use in LSC devices and characterization.[60] ^{1}H NMR confirms purity postpurification as no contamination of starting materials is apparent (Figure S4). Shown in Figures 4A and 4B are the ^{1}H NMR of the free DDT and DDT-capped CIS/ZnS core/shell QDs acquired in CD$_2$Cl$_2$. Only six signals were found in the spectrum in Figure 4B which were in proportions which confirm that the majority of ligands on the QDs are thiol-bound DDT (see Figure 4A).[61] Most peaks exhibit significant broadening, indicative of the interaction of the DDT ligand with the QD, where signals from protons closest to the QD surface are broadest.[62,63] The peaks at δ = 0.88 and 1.26 ppm have relative areas of 3.0 and 15.74, which correspond to the methyl terminus and the eight adjacent methylenes to this end-group, respectively. The signals for the DDT protons closer to the QD surface are significantly broader and exhibit reduced intensity because of their restricted relaxation.[64,65] The peaks at δ = 1.54 and 1.82 ppm (Figure 4B) have a relative area of 2.00 and 2.15 and correspond to methylene units three and two carbons removed from the thiol terminus, respectively. The broad and weak signal at δ = 2.88 has an integral value of 1.92 and corresponds to the methylene unit alpha to the thiol group.

To quantify the composition of ligand-exchanged QDs, 1D and 2D ^{1}H NMR spectra of the BCP-capped QDs and pure ligands were compared. Shown in Figure 5C is the ^{1}H NMR of
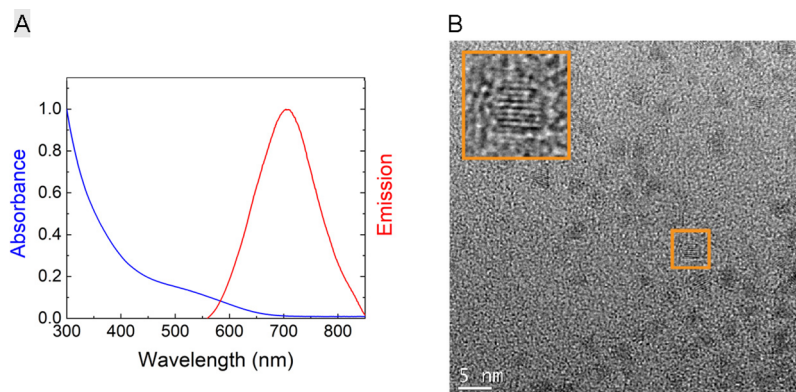
A

B

Figure 2. Normalized absorbance and emission spectra (A) and TEM image (B) of BCP-capped CIS/ZnS QDs.
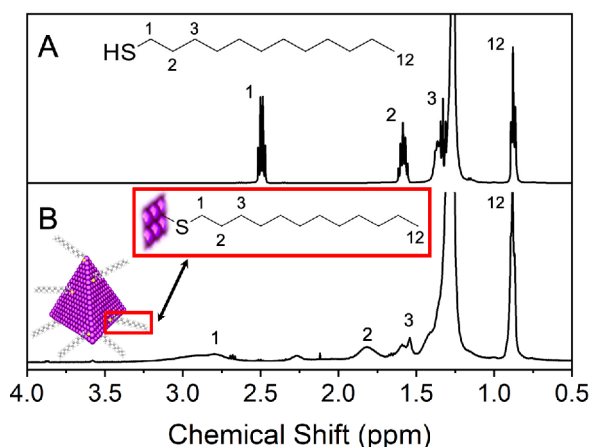
Figure 4. ^{1}H NMR spectra of free DDT (A) and DDT-capped CIS/ZnS QDs (B) dissolved in CD$_2$Cl$_2$. The ^{1}H NMR comparison shows two types of DDT features: sharp peaks characteristics of the molecules in free solution and broadened peaks that associate with molecules bound to the QD surface. The collapse of resonance multiplicity, line broadening, and a difference in chemical shift indicate the thiol of DDT is terminally bound to QD surface.
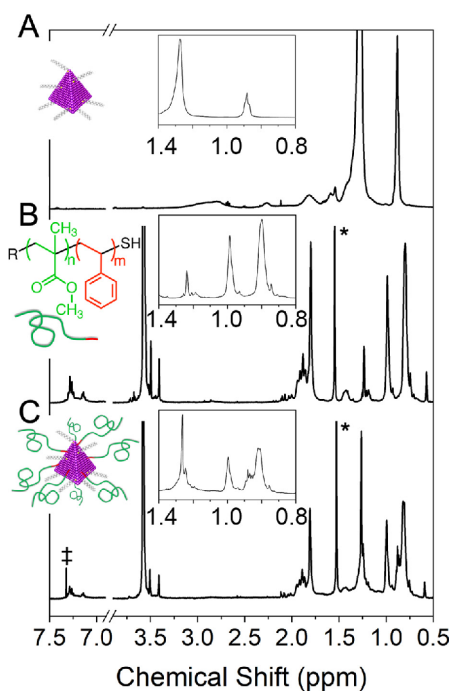

Figure 5. 1D ^{1}H NMR stack plot of (A) DDT-capped CIS/ZnS QDs, (B) free α-phenyl-ω-thio-PMMA-b-PS BCP ligands, and (C) α-phenyl-ω-thio-PMMA-b-PS BCP-capped CIS/ZnS QDs. The symbols $*$ and $\ddagger$ indicate signals from water and chloroform, respectively.

the BCP-capped QDs in CD$_2$Cl$_2$ solvent, selected because of its higher dielectric constant so as to minimize overlap in the −CH$_2$ and −CH$_3$ region for this study. The 1D ^{1}H NMR spectrum consists of signals similar to those assigned to the starting materials but exhibited some subtle differences. Peaks for DDT (at δ = 0.88 and 1.27 ppm) were found, confirming that the ligand exchange produced a CIS/ZnS QD with a mixed-ligand surface.

To determine the extent of conversion from DDT-capped QDs to PMMA-b-PS BCP-capped QDs, the integration of the tacticity options for the PMMA methyl groups need to be

examined.[66] Shown in Figure 5A−C are the ^{1}H NMR spectra for DDT-capped QDs and the free and QD-bound α-phenyl-ω-thio-PMMA-b-PS BCP, respectively. Peaks corresponding to −CH$_3$ and −CH$_2$ protons for DDT at δ = 0.88 and 1.27 ppm (Figure 5A), respectively, coincide with the signals for rr and mm triads for the tacticity options for the methyl groups in the QD-bound PMMA (δ = 0.81 and 1.24 ppm, respectively; Figure 5B). The mr triad peak at δ = 0.99 ppm is resolved from each of these other signals. The area ratio of rr:mr:mm in the spectrum for α-phenyl-ω-thio-PMMA-b-PS BCP is 4.71:2.36:1, which agrees with the literature.[66] By assuming that the total peak area of an overlapped peak is the sum of areas from components of DDT and those for certain polymer tacticity options, the BCP peak area can be extracted from the spectrum in Figure 5C and used to estimate the ratio of DDT and BCP bound to each QD. A typical batch of ligand exchanged QDs yields about 1.6 DDT ligands per 1 PMMA-b-PS BCP ligand, giving an overall conversion of 39%.

One-dimensional (1D) ^{1}H NMR spectroscopy techniques do not allow one to unequivocally distinguish between bound and free ligands. Diffusion-ordered NMR spectroscopy (DOSY) and nuclear Overhauser effect spectroscopy (NOESY) are useful for proving attachment of organic molecules to a QD surface.[67] The NOESY NMR spectra of free DDT and DDT-capped CIS/ZnS QDs in CDCl$_3$ are depicted in Figure 6, respectively. For small molecules, NOE
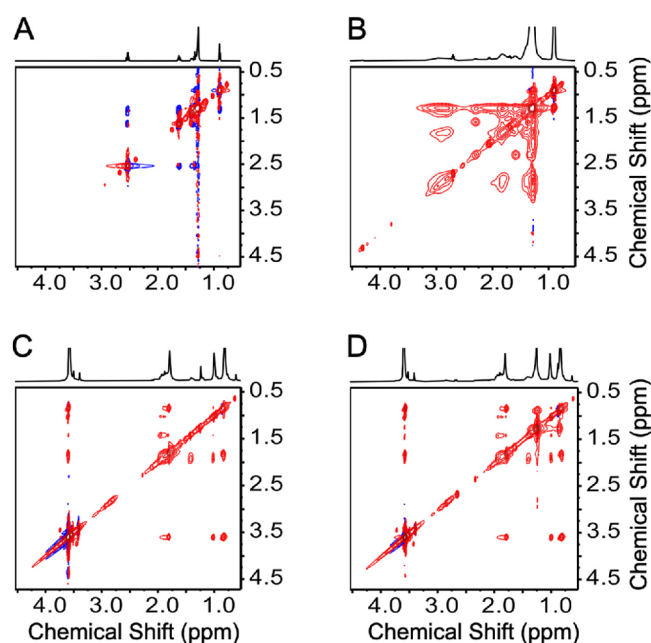

Figure 6. NOESY NMR spectra of (A) DDT, (B) DDT-capped CIS/ZnS QDs, (C) free PMMA-b-PS BCP ligands, and (D) PMMA-b-PS BCP-capped CIS/ZnS QDs. Spectra were acquired in CDCl$_3$, and red and blue contours denote positive and negative signal intensity, respectively.

cross-peaks have opposite phase to peaks found along the diagonal whereas signals for molecules bound to larger structures exhibit matched phase to those positioned on the diagonal. A weak NOE is apparent in the spectrum of free-DDT (Figure 6A), confirming that molecular diffusion is relatively fast for these fully solvated, unbound ligands. In contrast, the spectrum of QD-bound DDT in Figure 6B exhibits a large buildup of NOE cross peaks where enhanced

through-space dipole−dipole coupling between protons within the same immobilized molecule occurs under restricted diffusive motion. The NOESY spectra for the unbound and QD-bound PMMA-*b*-PS BCP ligand are shown in Figures 6C and 6D, respectively. Methyl and methylene peaks at 0.75−1.5 ppm exhibit peak broadening and stronger cross-peak intensity in Figure 6D, indicating increased through-space coupling compared to unbound molecules (Figure 6C).

Diffusion-ordered NMR spectroscopy (DOSY) experiments were also conducted to investigate the association of BCP ligands with CIS/ZnS QDs. Shown in Figure 7A is the DOSY
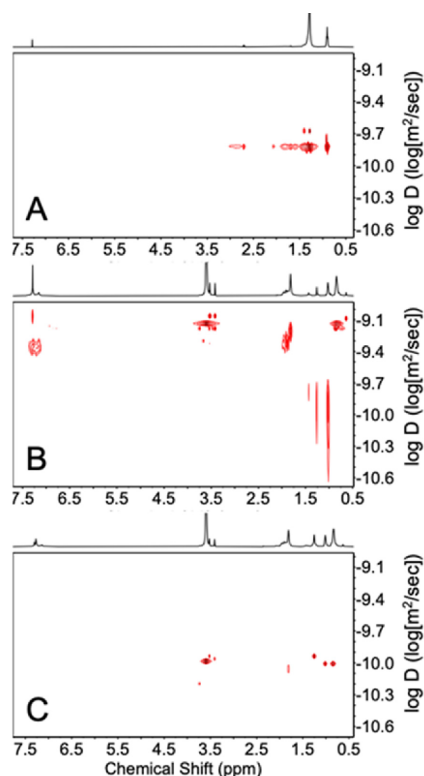

Figure 8. TGA of (A) α-phenyl-ω-thio-PMMA-*b*-PS BCP (CY$_{600}$ = 0.25%), (B) DDT-capped QDs (CY$_{600}$ = 53.5%), and (C) PMMA-*b*-PS BCP-capped QDs (CY$_{600}$ = 9.16%).

BCP ligand. These results serve to further confirm that BCP ligands are strongly associated with the QD surface.

Differential scanning calorimetry (DSC) and thermogravimetric analysis (TGA) were used to determine glass transition temperatures (T_g) in selected samples and to quantify the number of DDT ligands on the DDT-capped CIS/ZnS QDs, respectively. DSC scans for DDT-capped CIS/ZnS QDs, α-phenyl-ω-thio-PMMA-*b*-PS BCP, and the PMMA-*b*-PS BCP-capped CIS/ZnS QDs are provided in Figure S5. No thermal transitions were detected for the DDT-capped CIS/ZnS QDs. A signal for a T_g in α-phenyl-ω-thio-PMMA-*b*-PS BCP material was found at 105 °C, close to that of PMMA (i.e., 111 °C).[68] The glass transition temperature for the BCP ligand was found to increase slightly for QD-bound molecules, to 108 °C. Because of the low number of repeat units of the PS component, no T_g signal for this polymer component is expected or observed.

Figure 8A presents mass loss data for α-phenyl-ω-thio-PMMA-*b*-PS BCP measured by TGA. A two-step mass loss profile is observed in this TGA plot with an onset temperature of 253 °C. The char yield at 600 °C for the sample was CY$_{600}$ = 0.25%, indicating near-quantitative volatilization of polymer decomposition products. The TGA mass loss profile for DDT-capped QDs is shown in Figure 8B. A single mass loss step is observed with an onset temperature of 295 °C and a char yield of 53.5%. Based on this mass loss, the average QD surface area of 29 nm^2 (computed for a tetrahedral shape with a mean edge length of 4.1 nm), and the density of CIS (4.75 g/cm^{3} [69]), there are ∼97 DDT ligands per QD, which correlates to a graft density σ_{DDT} = 3.39 ligands/nm^2.

The mass loss profile for BCP-capped QDs is depicted in Figure 8C, and similar to the free BCP, volatilization of decomposition products occurs over two main mass loss events. The onset temperature for mass loss and char yield were 258 °C and 9.16%, respectively. Assuming each QD has an average of 97 binding sites and based on the ligand exchange conversion determined by ¹H NMR (i.e., 39% of all sites occupied by BCP ligands) 59 DDT and 38 BCP ligands can be assigned to each QD. This corresponds to a polymer graft density of 1.24 chains/nm^2, which is in agreement with other recent work.[70]

Light-Scattering Losses in LSCs. To evaluate the effect of ligand substitution on optical scattering losses, a series of LSCs combining different ligands and polymer matrix materials

Figure 7. DOSY spectrum of DDT-capped QDs (A), free PMMA-*b*-PS BCP ligands (B), and PMMA-*b*-PS BCP-capped QDs (C) where the diffusion coefficients were calculated to be 2.571×10^{-6}, 5.542×10^{-6}, and 9.050×10^{-7} cm^2/s, respectively. The diffusion coefficient for the PMMA-*b*-PS BCP-capped QDs was found to be a magnitude smaller than the DDT-capped QDs.

spectrum for DDT-capped QDs in CDCl$_3$, from which a diffusion constant of 2.571×10^{-6} cm^2/s was determined. Assuming a hydrodynamic radius for the solvent $R_{H,S}$ = 0.15 nm, the hydrodynamic radius for DDT-capped QDs is estimated to be $R_{H,QD-DDT}$ = 2.0 nm by the Stokes−Einstein equation. Figure 7B presents the DOSY spectrum for free (unbound) α-phenyl-ω-thio-PMMA-*b*-PS BCP ligands in the same solvent. The diffusion constant and hydrodynamic radius were found to be 5.542×10^{-6} cm^2/s and 0.92 nm, respectively, as determined by averaging the values determined from −OCH$_3$ and −CH$_3$ side chains. Shown in Figure 8C is the DOSY spectrum for the BCP-capped QDs acquired in CDCl$_3$. The diffusion constant and hydrodynamic radius were found to be significantly larger than the precursor materials with values of 9.050×10^{-7} cm^2/s and 5.6 nm, respectively, again based on the −OCH$_3$ and −CH$_3$ signals for the bound
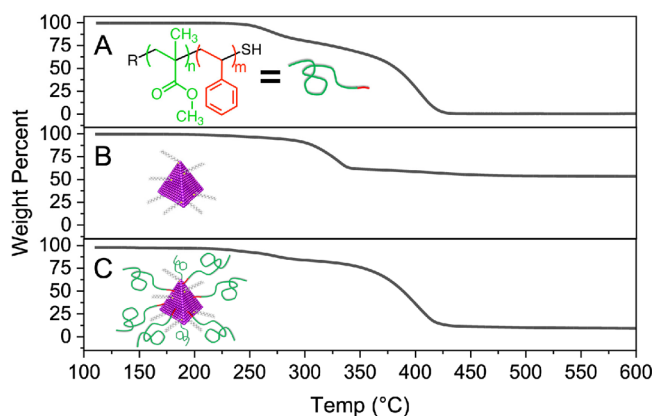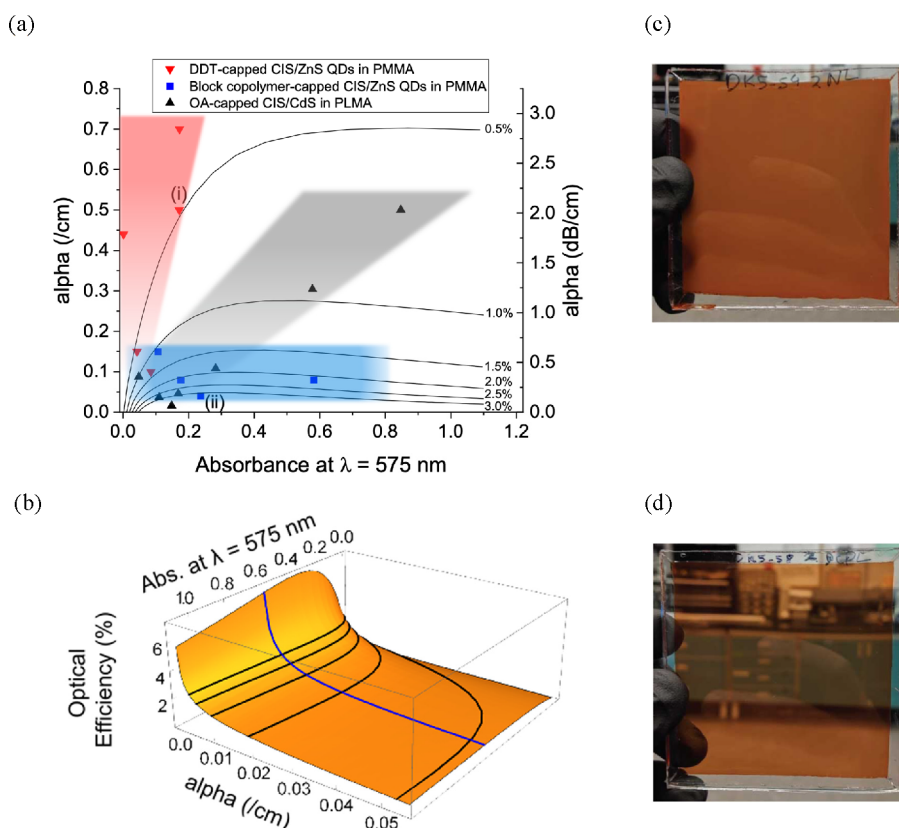
(a)

(c)

(b)

(d)

Figure 9. (a) Relationship between the attenuation loss rate α and optical density for several classes of LSCs. Three QD/polymer combinations are shown: (red) CuInS$_2$/ZnS-DDT in a PMMA waveguide, (blue) CuInS$_2$/ZnS-BCP in a PMMA waveguide, and (black) CuInS$_2$/CdS−OA in a PLMA waveguide reproduced and plotted from a previous work.[49] Contours denote constant-efficiency isolines for an idealized 50 × 50 cm^2 LSC with $\Phi = 1$ under AM 1.5G incident illumination. Shaded regions in the plot denote general ranges for α observed for each type of LSC. (b) 3-D plot depicting the relationship of absorbance (at λ = 575 nm), optical losses, and device performance. Photographs of devices represented by labels (i) and (ii) in (a) are shown in (c) and (d), respectively.

were fabricated and compared. LSC light-scattering losses can be determined several ways, including via haze and UV−vis absorption measurements performed at normal incidence to the major face of the device. However, because most applications envisioned for LSCs involve concentrator formats with a high geometric gain, G (where G is the ratio of the major facial area to total edge area), the relatively short path length sampled by these approaches makes their use for accurate determination of optical scattering losses challenging. Achieving practical levels of solar concentration in a high-G LSC requires a small attenuation coefficient, $\alpha \sim 1/L$, where L is the LSC edge length and the attenuation coefficient α is defined below. For example, a 50 × 50 cm^2 LSC requires $\alpha <$ ∼0.02 cm^{-1} over the wavelength window corresponding to peak QD emission.

To determine LSC losses due to scattering, we employed the analytical model of ref 49, which also accounts for self-absorption and nonunity PLQY losses. The first step in the analysis is to determine the portion of overall LSC extinction due to QD absorbance, which is done by fitting the extinction spectrum for each device with the function

$$\varepsilon_{\text{total}}(\lambda) = A\varepsilon_{\text{QD}}(\lambda) + B/\lambda^4 + C \tag{1}$$

where ε_{QD} is the normalized absorption spectrum of the QDs in toluene and A, B, and C are fitting constants representing QD absorption, scattering, and Fresnel reflections at the glass/air and glass/polymer interfaces. An example illustrating the

process is presented in Figure S6a. Corrected optical density (OD) values reported in the following are based on the best fit value of $A\varepsilon_{\text{NC}}(\lambda)$.

For an LSC illuminated at a single, small spot, the fraction of absorbed photons reaching a collection aperture at the edge of an LSC ("aperture internal photon efficiency", $\eta_{\text{int}}^{\text{ap}}$) can be calculated as a function of excitation distance from the integrated LSC absorbance and edge emission spectra. Precisely, $\eta_{\text{int}}^{\text{ap}}$ is the number of photons reaching the edge of the LSC at the aperture divided by the number of incident photons that are initially absorbed. We point out that in this work $\eta_{\text{int}}^{\text{ap}}$ is computed from monochromatic illumination and integration over all emitted wavelengths. The quantity $\eta_{\text{int}}^{\text{ap}}$ decreases with the distance d of the illumination point to the collection aperture due to a combination of escape cone, nonradiative relaxation, and waveguide attenuation losses as well as a geometric effect arising from the decrease in the in-plane collection angle subtended by the edge aperture with increasing d, which scales as $\tan^{-1}(1/d)$. Waveguide attenuation, or scattering losses, can be expressed as an optical path-length-dependent loss such that $P = P_0 e^{-\alpha\xi}$, where P/P_0 is the fraction of power remaining after a propagation distance ξ and α is the attenuation coefficient. The attenuation coefficient accounts for scattering by the polymer, scattering from QDs and QD aggregates, and polymer/glass as well as glass/air interfaces. Wavelength-dependent reabsorption by QDs and loss from less-than-unity PLQY are accounted for in the model but are separate from α. We approximate α as being

wavelength-independent over the emission band of the QDs. Assuming scattering at material interfaces is similar between devices and independent of QD loading, differences in the attenuation coefficient between devices can be attributed to differences in scattering from QD aggregates.

The discussion in the Supporting Information (Figure S6b) describes how α and Φ are determined for a representative device. Briefly, this is performed in two steps. First, the corrected optical density is determined by deconvolving the raw absorbance spectrum measured at normal incidence to the concentrator by using eq 1 (Figure S6a), as described above. Next, as shown in Figure S6b, calibrated edge emission intensity data are fit by using the attenuation model, yielding α and Φ. For further details refer to ref 49.

Figure 9 compares how scattering losses vary with QD loading in CIS-based LSCs employing three different QD dispersion strategies. One set of devices, shown in red, incorporated native DDT ligand CIS/ZnS QDs in PMMA. Poor chemical compatibility between the aliphatic ligands and polymer matrix results in QD aggregation and cloudy devices at concentrations too low for most practical applications (Figure 9c). A second set of devices from ref 49, shown in black, achieves improved performance by substituting poly-(lauryl methacrylate) (PLMA) for PMMA, increasing the compatibility between the LSC matrix and oleylamine (OA)-capped CIS/CdS QD luminophores. Compared to PMMA-based devices at similar loadings, reduced aggregation of oleophilic QDs in PLMA lowers scattering losses, though LSCs begin to become visibly cloudy above OD ∼ 0.4 (Figure 9a). LSCs incorporating BCP-capped CIS/ZnS QDs represent a third dispersion strategy, shown in blue. These devices are clear up to OD $\geq$ ∼0.6 (Figure 9d) and the scattering coefficient hardly changes with QD loading.

To illustrate the impact of α on concentrator performance, Figure 9b shows the predicted optical power efficiency (OPE) computed for a hypothetical 50×50 cm^2 LSC having the given {ABS, α}, and absorbance and emission spectra typical of those for the devices in Figure 9, under AM1.5G illumination. We consider OPE in this comparison (defined as the ratio of the total power of edge-emitted photons to the total power of photons incident on the LSC) because this quantity is intrinsic to the LSC and independent of the responsivity of edge-attached solar cells. To further isolate the effect of light scattering from other losses, we consider the limiting case where PLQY = 100%. In computing the OPE, edge-emitted light was approximated as monochromatic with λ = 675 nm, corresponding to the typical peak emission wavelength of the QDs synthesized in this work. Constant-OPE isolines from Figure 9b are overlaid in Figure 9a for reference. As noted above, achieving practical levels of performance in an LSC requires $\alpha < \sim 1/L < \sim 0.02$ cm^{-1} at a technologically relevant size scale, an order of magnitude lower than the most highly transparent devices in Figure 9, even though these devices appear visibly clear to the eye.

Highlighted in Figure 9b is a blue trace at a fixed absorbance of 0.58, a value that corresponds to that found for two devices reported in Figure 9a. These two devices consist of OA-capped CIS/CdS QDs in PLMA (black triangle) and BCP-capped CIS/ZnS QDs in PMMA (blue square). The blue curve allows for an estimate of the improvement of device performance by reducing α when the absorbance and other parameters are held constant (see Figure S7). For the two devices on this curve, that with BCP-capped CIS/ZnS QDs in PMMA had a predicted OPE of 1.83% while the corresponding OPE for the OA-capped CIS/CdS QD in PLMA was 0.76%. Thus, by reducing α, a 2.4-fold improvement in performance is predicted for a concentrator of the modeled size and PLQY. Even more significant, however, is that in contrast to devices based on the other two dispersion strategies illustrated in Figure 9, scattering in BCP-QD LSCs is independent of QD loading over range studied. Note that this range includes QD loadings (and hence optical densities) extending beyond the point corresponding to peak efficiency; that is, it encompasses the technologically relevant range for most anticipated applications. In addition, the observation that α is independent of loading in BCP-capped QDs indicates QD aggregation is not the main source of scattering losses in these devices, which increase approximately in proportion to the third power of QD loading when scattering from aggregates dominates.[49] Other phenomena, such as small entrapped bubbles, rough interfaces, and impurities, combined with the experimental challenge of measuring small scattering losses using relatively small devices, may be limiting instead, suggesting even higher performance may be achievable by combining ligand compatibilization strategies such as the one investigated here with improved fabrication techniques.

CONCLUSIONS

A primary advantage LSCs offer relative to conventional photovoltaic panels is transparency, which enables their use in building-integrated solar power production and other built-environment energy-harvesting applications. LSC-based windows, facades, skylights, and related concepts require partial transparency, with absorbance over visible wavelengths $\leq$ ∼0.5 AU in many practical contexts. Such applications also call for polymer waveguide and other materials with long outdoor lifetimes. Few polymers afford the same combination of high optical transparency, low cost, highly adaptable manufacturing modalities, and proven long-term outdoor performance as PMMA, which has been used in the building industry for decades. To realize PMMA-based LSCs with QD lumino-phores, the design, synthesis, and installation of PMMA-compatible ligands on the QDs was necessary. A PMMA BCP structure for the ligand was needed in this case, where a short segment of PS prevented a thiol backbiting side reaction that would otherwise consume the thiol termini reserved for binding to the QD surface. The complete molecular characterization by multidimensional NMR, GPC, DSC, and TGA of the BCP ligand and its CIS/ZnS QD derivative was reported. Data indicate that 39% of the original DDT ligands on the CIS/ZnS QDs can be substituted with the thiol-terminated PMMA-*b*-PS BCP derivatives. The BCP-capped CIS/ZnS QDs exhibited a T_g value close to that of pure PMMA and had a PLQY similar to that of the DDT-capped CIS/ZnS QDs. LSC devices composed of a matrix of PMMA with these BCP-capped CIS/ZnS QDs as luminophores were fabricated, and their optical properties were characterized. These data were interpreted and fit to a model that allowed for estimate of an attenuation coefficient, α, which accounts for absorbance and scattering by the polymer, QDs, QD aggregates, and interfaces at the polymer/glass, and glass/air boundaries. The PMMA/BCP-capped CIS/ZnS QD LSC is predicted to improve OPE by approximately 2.4× relative to an equivalent LSC with poorer ligand-matrix compatibility, and scattering losses were found to be independent of QD loading over a technologically relevant range of concentrations. The results reported here

therefore serve to demonstrate the potential for strategies based on compatibilizing ligands to achieve low scattering at technology-relevant QD loading in technology-relevant polymer materials.

ASSOCIATED CONTENT

Supporting Information

The Supporting Information is available free of charge at https://pubs.acs.org/doi/10.1021/acsapm.1c01837.

NOESY and DOSY program specifications and ^{1}H NMR spectra for thiolactone-terminated PMMA, selected starting materials and resulting DDT-capped CIS/ZnS QDs; GPC chromatograms for α-phenyl-ω-dithiobenzoyl-PMMA, α-phenyl-ω-dithiobenzoyl-PMMA-b-PS, and α-phenyl-ω-thio-PMMA-b-PS; TEM micrographs for DDT-capped CIS/ZnS QDs and BCP-capped QDs with size distribution histogram for the latter; DSC plots for DDT-capped CIS/ZnS QDs, α-phenyl-ω-thio-PMMA-b-PS and BCP-capped CIS/ZnS QDs; description of how α and Φ are determined for an LSC device and example data with deconvolution for absorbance of QDs in an LSC; plot for aperture internal photon efficiency", η_{int}^{ap}, vs excitation distance for an LSC device and a modeled OPE vs α loss parameter for devices with a fixed absorbance of 0.58 (PDF)

AUTHOR INFORMATION

Corresponding Author

David A. Rider − *Chemistry Department, Western Washington University, Bellingham, Washington 98225, United States; Department of Engineering and Design, Western Washington University, Bellingham, Washington 98225, United States;* orcid.org/0000-0002-8877-2069; Email: david.rider@wwu.edu

Authors

Kayla C. Koch − *Chemistry Department, Western Washington University, Bellingham, Washington 98225, United States*

Daniel Korus − *Chemistry Department, Western Washington University, Bellingham, Washington 98225, United States*

Justin Doyle − *Chemistry Department, Western Washington University, Bellingham, Washington 98225, United States*

Megan Plummer − *Chemistry Department, Western Washington University, Bellingham, Washington 98225, United States*

Meredith Boxx − *Chemistry Department, Western Washington University, Bellingham, Washington 98225, United States*

Hla Win-Piazza − *Chemistry Department, Western Washington University, Bellingham, Washington 98225, United States*

Stephen McDowall − *Department of Mathematics, Western Washington University, Bellingham, Washington 98225, United States*

David L. Patrick − *Chemistry Department, Western Washington University, Bellingham, Washington 98225, United States;* orcid.org/0000-0003-3543-9868

Complete contact information is available at:
https://pubs.acs.org/10.1021/acsapm.1c01837

Author Contributions

K.C.K. and D.K. contributed equally to this work.

Notes

The authors declare no competing financial interest.

REFERENCES

(1) Schreuder, M. A.; Gosnell, J. D.; Smith, N. J.; Warnement, M. R.; Weiss, S. M.; Rosenthal, S. J. Encapsulated white-light CdSe nanocrystals as nanophosphors for solid-state lighting. *J. Mater. Chem.* **2008**, *18*, 970−975.

(2) Fogg, D. E.; Radzilowski, L. H.; Dabbousi, B. O.; Schrock, R. R.; Thomas, E. L.; Bawendi, M. G. Fabrication of Quantum Dot-Polymer Composites: Semiconductor Nanoclusters in Dual Function Ploymer Matrices with Electron-Transporting and Cluster-Passivating Properties. *Macromolecules* **1997**, *30*, 8433−8439.

(3) Tomczak, N.; Janczewski, D.; Han, M.; Vancso, G. J. Designer Polymer-Quantum Dot Architectures. *Prog. Polym. Sci.* **2009**, *34*, 393−430.

(4) Kang, Z.; Zhang, Y.; Menkara, H.; Wagner, B. K.; Summers, C. J.; Lawrence, W.; Nagarkar, V. CdTe quantum dots and polymer nanocomposites for X-ray scintillation and imaging. *Appl. Phys. Lett.* **2011**, *98*, 1819141−1819143.

(5) Guerreiro, P. T.; Ten, S.; Borrelli, N. F.; Butty, J.; Jabbour, G. E.; Peyghambarian, N. PbS quantum-dot doped glasses as saturable absorbers for mode locking of a Cr:forsterite laser. *Appl. Phys. Lett.* **1997**, *71*, 1595−1597.

(6) Schaller, R. D.; Petruska, M. A.; Klimov, V. I. Tunable near-infrared optical gain and amplified spontaneous emission using pbse nanocrystals. *J. Phys. Chem. B* **2003**, *107*, 13765−13768.

(7) Sukhovatkin, V.; Musikhin, S.; Gorelikov, I.; Cauchi, S.; Bakueva, L.; Kumacheva, E.; Sargent, E. Room temperature amplified spontaneous emission at 1300 nm in solution-processed PbS quantum-dot films. *Opt. Lett.* **2005**, *30*, 171−173.

(8) Colvin, V.; Schlamp, M.; Alivisatos, A. Light-emitting diodes made from cadmium selenide nanocrystals and a semiconducting polymer. *Nature* **1994**, *370*, 354−357.

(9) Tessler, N.; Medvedev, V.; Kazes, M.; Kan, S.; Banin, U. Efficient near-infrared polymer nanocrystal light-emitting diodes. *Science* **2002**, *295*, 1506−1508.

(10) Shirasaki, Y.; Supran, G. J.; Bawendi, M. G.; Bulović, V. Emergence of colloidal quantum-dot light-emitting technologies. *Nat. Photonics* **2013**, *7*, 13−23.

(11) Weber, W. H.; Lambe, J. Luminescent greenhouse collector for solar radiation. *Appl. Opt.* **1976**, *15*, 2299−2300.

(12) Goetzberger, A.; Greube, W. Solar energy conversion with fluorescent collectors. *Appl. Phys. Lett.* **1977**, *14*, 123−139.

(13) Swanson, R. M. The Promise of Concentrators. *Prog. Photo. Res. Appl.* **2000**, *8*, 93−111.

(14) Verbunt, P. P. C.; Debije, M. G. Progress in Luminescent Solar Concentrator Research: Solar Energy for the Built Environment. *Proc. World Renewable Energy Congress Linköping, Sweden* **2011**, 2751−2759.

(15) Kurtz, S. Opportunities and Challenges for Development of a Mature Concentrating Photovoltaic Power Industry. *Nat. Ren. Energy Lab. Technol. Rep. NREL/TP 5200-43208* **2008**.

(16) Smestad, G.; Ries, H.; Winston, R.; Yablonovitch, E. The thermodynamic limits of light concentrators. *Sol. Energy Mater.* **1990**, *21*, 99−111.

(17) Ries, H. Thermodynamic limitations of the concentration of electromagnetic radiation. *J. Opt. Soc. Am. A* **1982**, *72*, 380−385.

(18) Papakonstantinou, I.; Tummeltshammer, C. Fundamental limits of concentration in luminescent solar concentrators revised: the effect of reabsorption and nonunity quantum yield. *Optica* **2015**, *2*, 841−849.

(19) Van Sark, W. G. J. H. M.; Barnham, K. W. J.; Slooff, L. H.; Chatten, A. J.; Büchtemann, A.; Meyer, A.; McCormack, S. J.; Koole, R.; Farrell, D. J.; Bose, R.; Beude, E. E.; Burgers, A. R.; Budel, T.; Quilitz, J.; Kennedy, M.; Meyer, T.; De Mello Donegà, C.; Meijerink, A.; Vanmaekelbergh, D. Luminescent Solar Concentrators - A review of recent results. *Opt. Express* **2008**, *16*, 21773−21792.

(20) Batchelder, J. S.; Zewai, A. H.; Cole, T. Luminescent solar concentrators. 1: Theory of operation and techniques for performance evaluation. *Appl. Opt.* **1979**, *18*, 3090−3110.

(21) Debije, M. G.; Verbunt, P. P. C. Thirty Years of Luminescent Solar Concentrator Research: Solar Energy for the Build Environment. *Adv. Energy Mater.* **2012**, *2*, 12−35.

(22) Li, Y.; Zhang, X.; Zhang, Y.; Dong, R.; Luscombe, C. K. Review on the Role of Polymers in Luminescent Solar Concentrators. *Polym. Chem.* **2019**, *57*, 201−215.

(23) Zhao, Y.; Meek, G. A.; Levine, B. G.; Lunt, R. R. Light Harvesting: Near-Infrared Harvesting Transparent Luminescent Solar Concentrators. *Adv. Opt. Mater.* **2014**, *2*, 606−611.

(24) Sanguineti, A.; Sassi, M.; Turrisi, R.; Ruffo, R.; Vaccaro, G.; Meinardi, F.; Beverina, L. High Stokes shift perylene dyes for luminescent solar concentrators. *Chem. Commun.* **2013**, *49*, 1618−1620.

(25) Currie, M. J.; Mapel, J. K.; Heidel, T. D.; Goffri, S.; Baldo, M. A. High-efficiency organic solar concentrators for photovoltaics. *Science* **2008**, *321*, 226−228.

(26) Banal, J. L.; Ghiggino, K. P.; Wong, W. W. H. Efficient light harvesting of a luminescent solar concentrator using excitation energy transfer from an aggregation-induced emitter. *Phys. Chem. Chem. Phys.* **2014**, *16*, 25358−25363.

(27) Reisfeld, R.; Kalisky, Y. Improved planar solar converter based on uranyl neodymium and holmium glasses. *Nature* **1980**, *283*, 281−282.

(28) Levin, M. B.; Starostina, G. P.; Cherkasov, G. P. Efficiency of solar concentrators based on luminescent silicone glasses. *Zhurn. Prikl. Spektrosk.* **1987**, *46*, 432−437.

(29) Wang, T.; Zhang, J.; Ma, W.; Luo, Y.; Wang, L.; Hu, Z.; Wu, W.; Wang, X.; Zou, G.; Zhang, Q. Luminescent solar concentrator employing rare earth complex with zero self-absorption loss. *Sol. Energy* **2011**, *85*, 2571−2579.

(30) Sanguineti, A.; Monguzzi, A.; Vaccaro, G.; Meinardi, F.; Ronchi, E.; Moret, M.; Cosentino, U.; Moro, G.; Simonutti, R.; Mauri, M.; Tubino, R.; Beverina, L. NIR emitting ytterbium chelates for colourless luminescent solar concentrators. *Phys. Chem. Chem. Phys.* **2012**, *14*, 6452−6455.

(31) Alghamedi, R.; Vasiliev, M.; Nur-E-Alam, M.; Alameh, K. Spectrally-selective all-inorganic scattering luminophores for solar energy-harvesting clear glass windows. *Sci. Rep.* **2015**, *4*, 6632−6639.

(32) Inman, R. H.; Shcherbatyuk, G. V.; Medvedko, D.; Gopinathan, A.; Ghosh, S. Cylindrical luminescent solar concentrators with near-infrared quantum dots. *Opt. Express* **2011**, *19*, 24308−24313.

(33) Barnham, K.; Marques, J. L.; Hassard, J.; O'Brien, P. Quantum-dot concentrator and thermodynamic model for the global red-shift. *Appl. Phys. Lett.* **2000**, *76*, 1197−1199.

(34) Purcell-Milton, F.; Gun'ko, Y. K. J. Quantum dots for Luminescent Solar Concentrators. *J. Mater. Chem.* **2012**, *22*, 16687−16697.

(35) Wang, C.; Winston, R.; Zhang, W.; Pelka, D.; Carter, S. Size- and structure-dependent efficiency enhancement for luminescent solar concentrators. *J. Photon. Energy* **2011**, *1*, 0155021−0155028.

(36) Bomm, J.; Buchtemann, A.; Chatten, A. J.; Bose, R.; Farrell, D. J.; Chan, N. L. A.; Xiao, Y.; Slooff, L. H.; Meyer, T.; Meyer, A.; van Sark, W. G. J. H. M.; Koole, R. Fabrication and full characterization of state-of-the-art quantum dot luminescent solar concentrators. *Sol. Energy Mater. Sol. Cells.* **2011**, *95*, 2087−2094.

(37) Gallagher, S. J.; Rowan, B. C.; Doran, J.; Norton, B. Quantum dot solar concentrator: Device optimization using spectroscopic techniques. *Sol. Energy* **2007**, *81*, 540−547.

(38) Zhou, Y.; Benetti, D.; Fan, Z.; Zhao, H.; Ma, D.; Govorov, A. O.; Vomiero, A.; Rosei, F. Near Infrared, High Efficient Luminescent Solar Concentrators. *Adv. Energy Mater.* **2016**, *6*, 1501913−1501921.

(39) Coropceanu, I.; Bawendi, M. G. Core/Shell Quantum Dot Based Luminescent Solar Concentrators with Reduced Reabsorption and Enhanced Efficiency. *Nano Lett.* **2014**, *14*, 4097−4101.

(40) Meinardi, F.; Colombo, A.; Velizhanin, K. A.; Simonutti, R.; Lorenzon, M.; Beverina, L.; Viswanatha, R.; Klimov, V. I.; Brovelli, S. Large-area luminescent solar concentrators based on Stokes-shift-engineered nanocrystals in a mass-polymerized PMMA matrix. *Nat. Photonics* **2014**, *8*, 392−399.

(41) Bronstein, N. D.; Yao, Y.; Xu, L.; O'Brien, E.; Powers, A. S.; Ferry, V. E.; Alivisatos, P. A.; Nuzzo, R. G. Quantum Dot Luminescent Concentrator Cavity Exhibiting 30-fold Concentration. *ACS. Photon.* **2015**, *2*, 1576−1583.

(42) Bronstein, N. D.; Li, L.; Xu, L.; Yao, Y.; Ferry, V. E.; Alivisatos, A. P.; Nuzzo, R. G. Luminescent solar concentration with semiconductor nanorods and transfer-printed micro-silicon solar cells. *ACS Nano* **2014**, *8*, 44−53.

(43) Hu, X.; Kang, R.; Zhang, Y.; Deng, L.; Zhong, H.; Zou, B.; Shi, L. J. Ray-trace simulation of CuInS(Se)2 quantum dot based luminescent solar concentrators. *Opt. Expr.* **2015**, *23*, A858−A867.

(44) Bradshaw, L. R.; Knowles, K. E.; McDowall, S.; Gamelin, D. R. Nanocrystals for Luminescent Solar Concentrators. *Nano Lett.* **2015**, *15*, 1315−1323.

(45) Knowles, K. E.; Kilburn, T. B.; Alzate, D. G.; McDowall, S.; Gamelin, D. R. Bright CuInS2/CdS nanocrystal phosphors for high-gain full-spectrum luminescent solar concentrators. *Chem. Commun.* **2015**, *51*, 9129−9132.

(46) Meinardi, F.; McDaniel, H.; Carulli, F.; Colombo, A.; Velizhanin, K. A.; Makarov, N. S.; Simonutti, R.; Klimov, V. I.; Brovelli, S. Highly Efficient Large-Area Colourless Luminescent Solar Concentrators Using Heavy-Metal-Free Colloidal Quantum Dots. *Nat. Nanotechnol.* **2015**, *10*, 878−885.

(47) Li, C.; Chen, W.; Wu, D.; Quan, D.; Zhou, Z.; Hao, J.; Qin, J.; Li, Y.; He, Z.; Wang, K. Large Stokes Shift and High Efficiency Luminescent Solar Concentrator Incorporated with CuInS2/ZnS Quantum Dots. *Sci. Rep.* **2016**, *5*, 177771−177779.

(48) Klimov, V. I.; Baker, T. A.; Lim, J.; Velizhanin, K. A.; McDaniel, H. Quality Factor of Luminescent Solar Concentrators and Practical Concentration Limits Attainable with Semiconductor Quantum Dots. *ACS Photonics* **2016**, *3*, 1138−1148.

(49) Sumner, R.; Eiselt, S.; Kilburn, T. B.; Erickson, C.; Carlson, B.; Gamelin, D. R.; McDowall, S.; Patrick, D. L. Analysis of Optical Losses in High-Efficiency CuInS2-Based Nanocrystal Luminescent Solar Concentrators: Balancing Absorption versus Scattering. *J. Phys. Chem. C* **2017**, *121*, 3252−3260.

(50) Koerner, H.; Drummy, L. F.; Benicewicz, B.; Li, Y.; Vaia, R. A. Nonisotropic Self-Organization of Single-Component Hairy Nano-particle Assemblies. *ACS Macro Lett.* **2013**, *2*, 670−676.

(51) Li, L.; Pandey, A.; Werder, D. J.; Khanal, B. P.; Pietryga, J. M.; Klimov, V. I. Efficient Synthesis of Highly Luminescent Copper Indium Sulfide-Based Core/Shell Nanocrystals with Surprisingly Long-Lived Emission. *J. Am. Chem. Soc.* **2011**, *133*, 1176−1179.

(52) Xu, J.; He, J.; Fan, D.; Wang, X.; Yang, Y. Aminolysis of Polymers with Thiocarbonylthio Termini Prepared by RAFT Polymerization: The Difference between Polystyrene and Polymethacrylates. *Macromolecules* **2006**, *39*, 8616−8624.

(53) Draaisma, G.; Reardon, D.; Schenning, A.; Meskers, S.; Bastiaansen, C. Ligand exchange as a tool to improve quantum dot miscibility in polymer composite layers used as luminescent down-

shifting layers for photovoltaic applications. *J. Mater. Chem. C* **2016**, *4*, 5747−5754.

(54) Yang, C. C.; Atwater, H. A.; Baldo, M. A.; Baran, D.; Barile, C. J.; Barr, M. C.; Bates, M.; Bawendi, M. G.; Bergren, M. R.; Borhan, B.; Brabec, C. J.; Brovelli, S.; Bulovic, V.; Ceroni, P.; Debije, M. G.; Delgado-Sanchez, J. M.; Dong, W. J.; Duxbury, P. M.; Evans, R. C.; Forrest, S. R.; Gamelin, D. R.; Giebink, N. C.; Gong, X.; Griffini, G.; Guo, F.; Herrera, C. K.; Ho-Baillie, A. W. Y.; Holmes, R. J.; Hong, S. K.; Kirchartz, T.; Levine, B. G.; Li, H. B.; Li, Y. L.; Liu, D. Y.; Loi, M. A.; Luscombe, C. K.; Makarov, N. S.; Mateen, F.; Mazzaro, R.; McDaniel, H.; McGehee, M. D.; Meinardi, F.; Menendez-Velazquez, A.; Min, J.; Mitzi, D. B.; Moemeni, M.; Moon, J. H.; Nattestad, A.; Nazeeruddin, M. K.; Nogueira, A. F.; Paetzold, U. W.; Patrick, D. L.; Pucci, A.; Rand, B. P.; Reichmanis, E.; Richards, B. S.; Roncali, J.; Rosei, F.; Schmidt, T. W.; So, F.; Tu, C. C.; Vahdani, A.; van Sark, W.; Verduzco, R.; Vomiero, A.; Wong, W. W. H.; Wu, K. F.; Yip, H. L.; Zhang, X. W.; Zhao, H. G.; Lunt, R. R. Consensus statement: Standardized reporting of power-producing luminescent solar concentrator performance. *Joule* **2022**, *6*, 8−15.

(55) Roth, P. J.; Kessler, D.; Zentel, R.; Theato, P. A Method for Obtaining Defined End Groups of Polymethacrylates Prepared by the RAFT Process during Aminolysis. *Macromolecules* **2008**, *41*, 8316−8319.

(56) McCormick, C. L.; Lowe, A. B. Aqueous RAFT Polymerization: Recent Developments in Synthesis of Functional Water-Soluble (Co)polymers with Controlled Structures. *Acc. Chem. Res.* **2004**, *37*, 312−325.

(57) Sasso, B.; Dobinson, M.; Hodge, P.; Wear, T. Synthesis of *ω*-End Group Functionalized Poly(methyl methacrylate)s via RAFT Polymerization. *Macromolecules* **2010**, *43*, 7453−7464.

(58) Yao, J.; Rudyk, B. W.; Brunetta, C. D.; Knorr, K. B.; Figore, H. A.; Mar, A.; Aitken, J. A. Mn incorporation in CuInS2 chalcopyrites: Structure, magnetism and optical properties. *Mater. Chem. Phys.* **2012**, *136*, 415.

(59) Jang, E.-P.; Song, W.-S.; Lee, K.-H.; Yang, H. Preparation of a photo-degradation- resistant quantum dot-polymer composite plate for use in the fabrication of a high-stability white-light-emitting diode. *Nanotechnology* **2013**, *24*, 0456071−0456079.

(60) Shen, Y.; Gee, M. Y.; Tan, R.; Pellechia, P. J.; Greytak, A. B. Purification of Quantum Dots by Gel Permeation Chromatography and the Effect of Excess Ligands on Shell Growth and Ligand Exchange. *Chem. Mater.* **2013**, *25*, 2838−2848.

(61) Ling, X.; Schaeffer, N.; Roland, S.; Pileni, M.-P. Superior Oxygen Stability of N-Heterocyclic Carbene-Coated Au Nanocrystals: Comparison with Dodecanethiol. *Langmuir* **2015**, *31*, 12873−12882.

(62) Houck, D. W.; Korgel, B. A. Facile Exchange of Tightly Bonded L-Type Oleylamine and Diphenylphosphine Ligands on Copper Indium Diselenide Nanocrystals Mediated by Molecular Iodine. *Chem. Mater.* **2018**, *30*, 8359−8367.

(63) Anderson, N. C.; Hendricks, M. P.; Choi, J. J.; Owen, J. S. Ligand Exchange and the Stoichiometry of Metal Chalcogenide Nanocrystals: Spectroscopic Observation of Facile Metal-Carboxylate Displacement and Binding. *J. Am. Chem. Soc.* **2013**, *135*, 18536−18548.

(64) Shon, Y.-S.; Gross, S. M.; Dawson, B.; Porter, M.; Murray, R. W. Alkanethiolate-Protected Gold Clusters Generated from Sodium S-Dodecylthiosulfate (Bunte Salts). *Langmuir* **2000**, *16*, 6555−6561.

(65) Canzi, G.; Mrse, A. A.; Kubiak, C. P. Diffusion-Ordered NMR Spectroscopy as a Reliable Alternative to TEM for Determining the Size of Gold Nanoparticles in Organic Solutions. *J. Phys. Chem. C* **2011**, *115*, 7972−7978.

(66) Miao, X.; Li, J.; Zhang, Z.; Cheng, Z.; Zhang, W.; Zhu, J.; Zhu, X. Dimanganese Decacarbonyl/2-Cyanoprop-2-Yl-1-Dithionaphthalate: Toward Sunlight Induced RAFT Polymerization of MMA. *Polym. Chem.* **2014**, *5*, 4641−4648.

(67) Morris-Cohen, A. J.; Malicki, M.; Peterson, M. D.; Slavin, J. W. J.; Weiss, E. A. Chemical, Structural, and Quantitative Analysis of the Ligand Shells of Colloidal Quantum Dots. *Chem. Mater.* **2013**, *25*, 1155−1165.

(68) Brandrup, J.; Immergut, E. H.; Grulke, E. A. *Polymer Handbook*, 4th ed.; Wiley: New York, 1999.

(69) Lefrançois, A.; Luszczynska, B.; Pepin-Donat, B.; Lombard, C.; Bouthinon, B.; Verilhac, J.-M.; Gromova, M.; Faure-Vincent, J.; Pouget, S.; Chandezon, F.; Sadki, S.; Reiss, P. Enhanced Charge Separation in Ternary P3HT/PCBM/CuInS2 Nanocrystals Hybrid Solar Cells. *Sci. Rep.* **2015**, *5*, 77681−77688.

(70) Ohno, K.; Koh, K.; Tsujii, Y.; Fukuda, T. Fabrication of Ordered Arrays of Gold Nanoparticles Coated with High- Density Polymer Brushes. *Angew. Chem., Int. Ed.* **2003**, *42*, 2751−2754.